Attitude Control for High Altitude Long Endurance Aircraft Considering Structural Load Limits

Christian Weiser* and Simon Schulz†
Institute of System Dynamics and Control, German Aerospace Center (DLR), 82234 Weßling, Germany

Arne Voß‡
Institute of Aeroelasticity, German Aerospace Center (DLR), 37073 Göttingen, Germany

Daniel Ossmann§
Department of Mechanical, Automotive and Aeronautical Engineering,
Munich University of Applied Sciences (HM), 80335 Munich, Germany

This paper presents the design of a flight control system (FCS) for the lateral axis of a very flexible High Altitude Long Endurance (HALE) aircraft. To ensure that the HALE aircraft stays within its defined flight envelope, the FCS design incorporates roll attitude tracking requirements in the form of a coordinated turn and disturbance rejection requirements in the form of adequate discrete gust and continuous turbulence mitigation. The HALE aircraft itself is prone to aeroelastic effects. The paper shows via an aeroelastic load analysis, that a FCS not explicitly considering loads in its design is insufficient, as peak loads in the fuselage torsion and vertical tail bending moment are increased. As a response to these findings, a design approach for lateral FCS is proposed, which allows to weight the structural loads at the vertical tail root against the maximum roll attitude during the gust encounter. The benefit of this control design may result either in a potential decrease in structural weight or strength margins of the fuselage. Finally, the resulting lateral axis FCS design is validated in non-linear simulations of lateral gust encounters and the reduction of maximum loads on the vertical tail during worst case gusts is shown.

I. Introduction

High Altitude Long Endurance (HALE) aircraft are typically designed for operation at altitudes of 18 - 25 km in the stratosphere. Mission scenarios for these aircraft are similar to those of satellites and require the platform to stay airborne in the stratosphere from multiple days up to several months. Furthermore, the platform shall be able to follow a desired ground track and perform multiple cycles from take-off to landing with the possibility of maintenance or exchange of its payload at relatively low cost. Staying airborne by using solar energy only requires extremely light weight structures. Compared to classical unmanned aerial vehicles, this results in high structural flexibility, a low tolerance on external (aerodynamic) loads and an unusually low (equivalent) airspeed for nominal operation.

In past projects, first flights of different HALE aircraft, as for example of the NASA HELIOS [1], failed, because HALE aircraft structures are very vulnerable to atmospheric disturbances. Recent advances in solar cell and battery technology as well as composite structures, however, allow a more feasible trade-off between structural weight, aspect ratio and flexibility of the structure today. In 2018, the Airbus Zephyr aircraft made its 30-day record flight [2] which proved the feasibility of the technology. The ultra light-weight structures and the operation at low airspeed, however, still pose problems in current research and development projects, especially in the aircraft verification against gust and turbulence encounters.

This paper uses the DLR's HAP platform [3] as an example with its initial control designs [4–6]. An artistic representation of the DLR HALE platform is shown in Fig. 1. The contribution of the paper is the analysis of structural loads resulting from external disturbances on the closed loop aircraft system and the incorporation of this knowledge into the Flight Control System (FCS) design. In former studies on HALE aircraft design it has been found that the sizing

---

[*] Research Associate, christian.weiser@dlr.de, AIAA Member

[†] Research Associate, simon.schulz@dlr.de

[‡] Research Scientist, arne.voss@dlr.de

[§] Professor, daniel.ossmann@hm.edu, AIAA Senior Member

Fig. 1 Exemplary HALE aircraft illustration (DLR).

of the rear fuselage is driven by bending and torsional loads from lateral gust encounters. Hence, the reduction of these loads by the FCS can facilitate also a reduction of the structural weight of the fuselage, which in turn is beneficial to achieve a very light-weight structure as described above. While most active load control and load alleviation activities focus on the wings, this work focuses on the vertical tail (VT) and the fuselage. This decision is made as in the case of DLR's HALE aircraft the lateral loads due to gust encounters are much higher than the maneuver loads, while for the wings maneuver and gust loads are nearly equal in magnitude. This knowledge is taken into account for re-design of an existing, initial inner loop roll attitude FCS. This novel inner loop design explicitly reduces the maximum root bending moment of the aircraft's VT during worst-case gust encounters. The method used for the re-design is a convex $\mathcal{H}_\infty$ control synthesis [7], where additional weights on the critical load stations are employed.

The first part of the paper introduces the DLR's HALE project with a focus on the aero-servo-elastic closed loop model. This includes the initial inner loop FCS [4] as well as a detailed aeroelastic model of the open loop aircraft and its dynamics [8, 9]. Thereafter, a summary of the loads analysis conducted by DLR's Institute of Aeroelasticity is presented, focusing on sizing load cases, e.g. load cases which coincide with a strong rigid body reaction to gusts. These load cases form the basis for the improvements by means of active load reduction. Using the results of this load analysis, the re-design of the roll attitude controller is performed. Therefore, the initially implemented control strategy which used weights on the rigid body outputs only is enhanced with a performance output specifically penalizing the VT root bending moment. In a final step, the obtained FCS is compared to the initial FCS for the most critical load case as well as for a sample size of 5000 different discrete 1-cosine gust encounter scenarios.

II. HALE Aircraft Dynamics and Initial FCS Design

This section provides an overview of the existing non-linear aircraft model [8, 10] and the model-based initial FCS which was previously presented in [4].

A. Non-linear Aircraft Model

The mathematical model of the HALE aircraft includes non-linear rigid body aircraft equations of motion [10, 11]

$$\begin{bmatrix} M_b(\dot{V}_b + \Omega_b \times V_b - T_{bE} g_E) \\ I_b(\dot{\Omega}_b + \Omega_b \times (I_b \Omega_b)) \end{bmatrix} = \Phi_{bg} P_g^{\text{ext}}, \tag{1}$$

with the aircraft's mass M_b, its moment of inertia I_b, and the translational and rotational velocities V_b and Ω_b. The gravitational acceleration vector g_E is transformed from the earth fixed coordinate system E to the body-fixed system b by the matrix T_{bE}. The model is augmented with a second order differential equation describing the flexible dynamics of the aircraft structure as described in e.g. [10] and [12]:

$$M_{ff}\ddot{u}_f + D_{ff}\dot{u}_f + K_{ff}u_f = \Phi_{fg} P_g^{\text{ext}}, \tag{2}$$

where u_f denotes the modal displacement. The matrices Φ_{bg} and Φ_{fg} are the modal transformation matrices from the structural grid (g-set) to the rigid body (b-set), respectively to the modal flexible coordinates (f-set). The mass matrix

M_{ff}, stiffness matrix K_{ff} and damping matrix D_{ff} are derived from model data (Fig. 2) provided by the DLR Institute of Aeroelasticity [9, 12, 13].

The external loads P_g^{ext} acting on the structural nodes (g-set) consist of aerodynamic loads P_g^{aero} and propulsion loads P_g^{prop}. The aerodynamic loads are derived by the vortex lattice method (VLM), which is based on potential flow theory. For more details the reader is referred to [14]. The internal structural loads (forces and moments) at specific monitoring stations (e.g. wing root) are calculated by applying the force summation method [14].

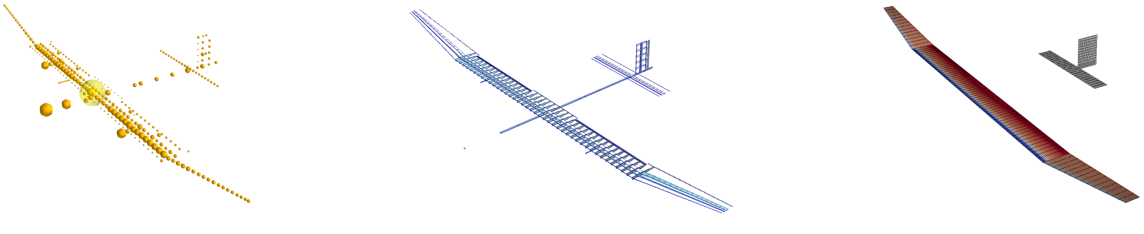
(a) (b) (c)

Fig. 2 Mass (Fig. 2a), structural (Fig. 2b) and aerodynamic panel (Fig. 2c) models of the DLR HALE aircraft.

B. Discrete Gust Input

The spatial wind velocity profile v_g of the discrete gust (1-cos shape) is defined by the certification requirements in CS/FAR 25.341 [15]:

$$v_g = \frac{1}{2} U_0 \left(1 - \cos\left(\frac{2\pi x_j}{2H}\right)\right), \tag{3}$$

where U_0 is the gust design velocity. For the HALE aircraft the expected worst case amplitudes are reduced to account for the planned flight time in combination with the probability of a worst-case gust encounter. The spatial coordinate x_j denotes the distance of each individual panel (j-set) w.r.t. the gust velocity profile v_g. The parameter H denotes the gust gradient and is defined between 9 and 107 meters according to [15]. The calculation of the aerodynamic loads due to the discrete gust is implemented as presented in [16, 17]. The result is applied to the model as an additional external load P_g^{ext}.

C. Initial Flight Control Design

Resulting from this non-linear, aeroelastic model, a linear model of the aircraft in the standard form

$$\left[\begin{array}{c} \dot{x} \\ \hline y \end{array}\right] = \left[\begin{array}{c|cc} A & B_u & B_d \\ \hline C & D_u & D_d \end{array}\right] \left[\begin{array}{c} x \\ \hline u \\ d \end{array}\right] \tag{4}$$

with the state vector x, it's derivative $\dot{x}$, the input vector u, the output vector y, the scalar disturbance d and the state space matrices A, B_u, B_d, C, D_u, and D_d, finally enables the application of a linear control design method. Therefore, the non-linear aircraft equations are linearized at a steady state operating point defined by equivalent airspeed V_{eas} and altitude h. A low order approximation of the aircraft's lateral dynamics is obtained via truncation of the longitudinal modes as well as flexible modes beyond the actuator bandwidth. For the derived aircraft model for the lateral controller design, the state vector x includes the angle of sideslip β, roll and yaw rate p and r, roll attitude ϕ, the involved structural modes U_f and their derivatives dU_f. The input vector u includes the aileron deflection ξ and rudder deflection ζ and the output vector y includes the rigid body states β, p, r, ϕ as well as the lateral acceleration n_y. The lateral acceleration is used as feedback variable instead of the angle of sideslip, as this variable is expected to have a more reliable and accurate measurement. Finally, the disturbance d is a wind disturbance on the aircraft.

For the lateral inner loop control, which is addressed in this work, a rate command attitude hold (RCAH) architecture has been selected [4]. The control architecture of the initial controller is depicted in Fig. 3. This architecture allows the pilot to command a roll rate during augmented flying, whereas the autopilot directly feeds a roll attitude command in case of activation of e.g. heading hold or path following operating mode. For the yaw axis, a second proportional-integral control structure was added, where the lateral acceleration reference $n_{\mathrm{y,\,cmd}}$ is set to zero at all times for coordinated maneuvering via the proportional and integral gains. Yaw damping via high-pass filtered yaw rate feedback is included as well. For development of the architecture, an eigenstructure assignment as discussed in [18, 19] is performed for linear models at selected operating points. These results show, that contrarily to lateral control for transport aircraft, the roll and yaw control should not be controlled separately, but there exists a strong cross coupling which also varies over the flight envelope parameters. As a result, the gains K_{pr} and K_{rp} are introduced into the control architecture to account for this effect. Afterwards, the synthesis of the structured, scheduled control law is formulated as an optimization problem as shown for this specific controller in [4] with a total of eight gains to be tuned (proportional, integral gains on the two tracking variables; proportional augmentation gains on rates; two cross-coupling gains; $K_{ff} = K_{D,\Phi}$). The optimization goals are derived from the tracking and disturbance rejection requirements described explained in Table 1.

Table 1 Roll attitude and turn coordination controller tuning specifications [4].

Name	Acceptable Value	Frequency Region
Roll attitude. bandwidth	2 rad/s	-
Lateral acceleration bandwidth	2 rad/s	-
Max. overshoot	3%	-
Gain / Phase Margin	6dB / 45 deg	[0; 4] rad/s
Gain / Phase Margin	8dB / 60 deg	]4; inf[rad/s
Dist. Rejection Roll	35 dB	[0; 1] rad/s
Dist. Rejection Yaw	20 dB	[0; 0.3] rad/s

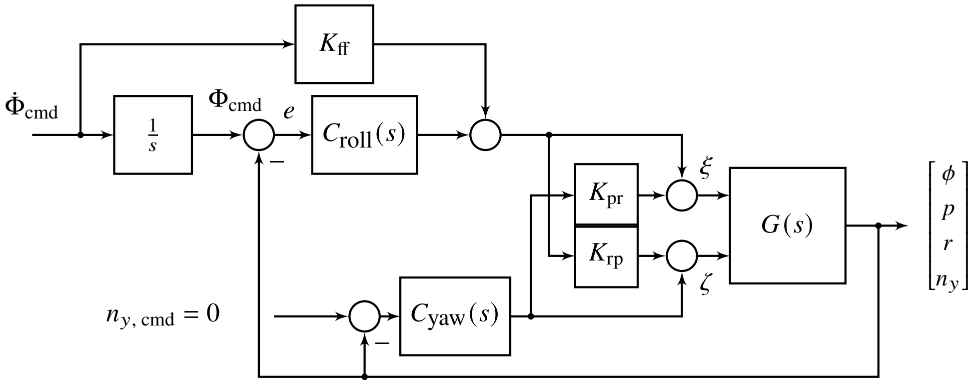

Fig. 3 Block diagram for fixed structure control design of a RCAH roll attitude controller with turn coordination by lateral acceleration feedback.

D. Loads Analysis of the Closed Loop Aircraft and Identification of Dimensioning Load Cases

During the loads analysis of the HALE configuration [8], multiple load cases are considered, including 1260 maneuver loads, 2016 1-cos gust encounters, 54 engine loads and 4 landing load cases. The highest resulting section loads are used for the sizing of the primary aircraft structure. For the wing, typical quantities are the bending moment M_x or the torsional moment M_y. Because a global coordinate system (aft-right-up) is used, the indices are switched for the fuselage so that M_x is a torsional moment and M_y is a bending moment. During the structural sizing, the laminate stacking and the ply angles of the individual layers can be adjusted either for better bending or for better torsional stiffness. A combined loading is more difficult and always requires a compromise, which typically results in higher structural mass. Looking at the rear fuselage bending and torsional moments M_y and M_x in Fig. 4a, it can be seen that the highest positive bending moment M_y is caused by both maneuver and gust load cases with $M_y = 380\,\mathrm{Nm}$ while the highest torsional moments M_x are dominated by gust load cases with $M_x = \pm\, 150\,\mathrm{Nm}$. The fuselage torsional moments can be tracked back to the forces and moments from the VT, which are shown in Fig. 4b. Looking at the VT root bending moment M_x and torsional moments M_z (mainly due to rudder deflections), the gust loads are again much higher compared to the maneuver loads. With $M_x = \pm 117\,\mathrm{Nm}$, the highest root bending moments are caused by a 9 m lateral 1-cosine gust (90/270°) at VC at sea level. Because of the large differences between maneuver and gust loads, a reduction of the gust loads at the VT by an improved flight controller would have a positive effect on both the VT and the fuselage. The VT primary structure is mainly sized by minimum wall thicknesses, but mass savings can be expected in the fuselage, due to lower torsional loads and by adjusting the laminate set-up.

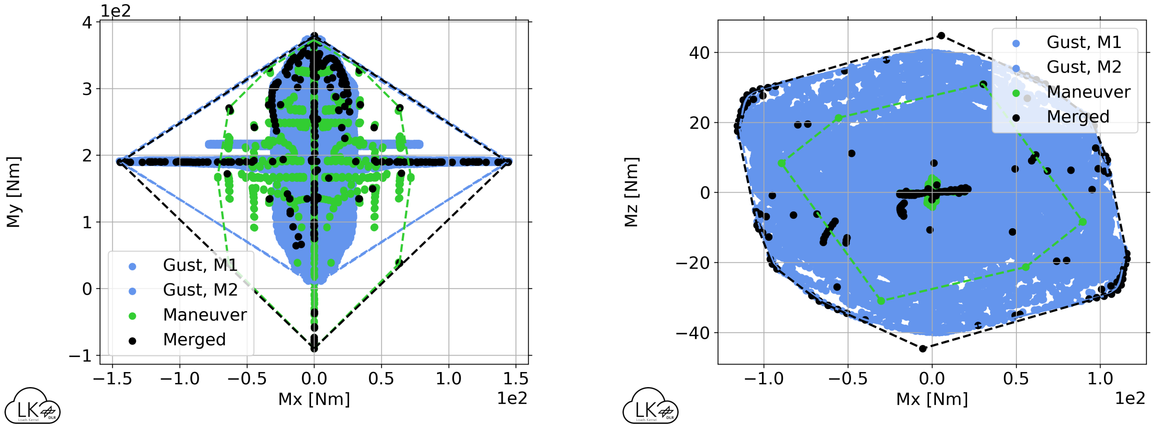

(a) **(b)**

Fig. 4 Rear fuselage bending and torsional moments M_y and M_x (Fig. 4a) and VT bending and torsional moments M_x and M_z (Fig. 4b).

III. Enhanced Roll Attitude Flight Control System Design

In contrast to the initial FCS described in Sec. II, a full order, convex $\mathcal{H}_\infty$ approach is chosen for the re-design. This is motivated by a further improvement which was observed compared to the structured $\mathcal{H}_\infty$ approach which can be traced down to the fixed and limited number of gains and integrators in this case. Instead of updating the controller structure and iterating multiple times, the full order $\mathcal{H}_\infty$ approach is able to obtain a more general result for the sake of giving up the fixed controller architecture. Both control design approaches work by shaping closed loop sensitivity functions through minimization of the $\mathcal{H}_\infty$-norm which is a common approach for control design in literature, see e.g. [20].

A common interconnection for designing the controller $K(s)$ is given in terms of a mixed sensitivity problem in Fig. 5 . The considered plant $G(s)$ can be augmented by an explicit disturbance model $G_d(s)$, as depicted in the figure. The mixed sensitivity formulation is the weighted closed loop system's $\mathcal{H}_\infty$-norm of the feedback interconnection in Fig. 5 [20], which can be noted as follows:

$$\begin{bmatrix} z_e \\ z_u \\ z_y \end{bmatrix} = \begin{bmatrix} W_e V_e^{-1} & 0 \\ 0 & W_u V_u^{-1} \\ W_y & 0 \end{bmatrix} \begin{bmatrix} S & -SG_d \\ KS & -KSG_d \end{bmatrix} \begin{bmatrix} V_e & 0 \\ 0 & W_d \end{bmatrix} \begin{bmatrix} r \\ d \end{bmatrix}, \tag{5}$$

where $S = (I + GK)^{-1}$ denotes the output sensitivity function. The weighting scheme differentiates between frequency dependent weights denoted by W and constant scaling factors denoted by V. It is taken from [21]. The weight function W_e enforces the frequency requirements on the sensitivity function, i.e. tracking and disturbance rejection at low frequencies. The weight W_u shapes the control input u through KS. It can be used to enforce an appropriate roll-off of the controller K. The scalings V_e, V_u and V_d can be used for setting the maximum allowable control error, control effort and disturbance, respectively.

For $\mathcal{H}_\infty$ feedback design, the weighting structure in Fig. 5 is transferred to the commonly known P-K structure [20], where the interconnection of the plant and weights is referred to as generalized plant P. The state-space realization of the generalized plant is given by Eq. (5). The loop transfer from $w = [r, \quad d]^T$ to $z = [z_e, \quad z_u, \quad z_y]^T$, can be rewritten as linear fractional transformation (LFT)

$$z = \mathcal{F}_{\mathcal{L}}(P, K)w \tag{6}$$

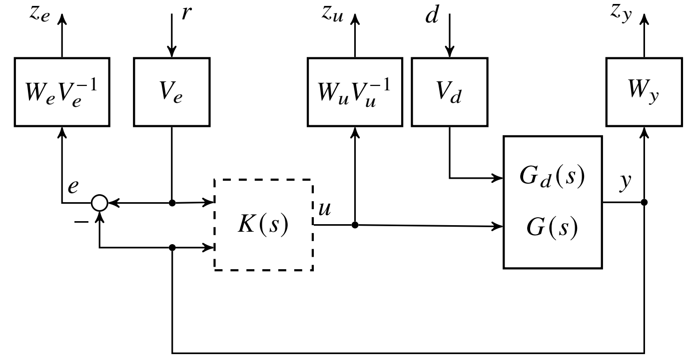

Fig. 5 Weighting Scheme of the $\mathcal{H}_\infty$ controller synthesis.

where

$$\mathcal{F}_\mathcal{L}(P,K) = P_{11} + P_{12}K(I - P_{22}K)^{-1}P_{21}. \tag{7}$$

For $\mathcal{H}_\infty$, the goal is to minimize the induced worst-case 2-norm of the transfer function from w to z, which corresponds to the LFT in Eq. (6). Before introducing an algorithm to solve the $\mathcal{H}_\infty$ problem, the assumptions need to be made [20]. One is the condition for the existence of a stabilizing controller K, whereas the second is sufficient to ensure that an existing controller is proper and stable. Moreover, the assumptions are needed to make sure the controller is not trying to cancel poles or zeros on the imaginary axis, which would lead to closed-loop instability. Referring to the general control configuration in Fig. 5, the $\mathcal{H}_\infty$ control problem is, to find all stabilizing controllers K, which minimize the signal transmission from w to z, or in other words

$$\|\mathcal{F}_\mathcal{L}(P,K)\|_\infty = \max_{w(t)\neq 0} \frac{\|z(t)\|_2}{\|w(t)\|_2}, \tag{8}$$

where $\|\cdot\|$ is the 2-norm of a vector signal. Minimizing the infinity norm represents minimizing the peak of the maximum singular value of $\mathcal{F}_\mathcal{L}(P,K)$. Time domain interpretation of this corresponds to the induced (worst-case) 2-norm. Note that in contrast to this, the optimal $\mathcal{H}_2$ control problem solves for the minimal root mean square of the output signal. In practice (e.g. because of computational reasons) it is often simpler to find a solution for a sub-optimal controller close to the minimal $\mathcal{H}_\infty$ norm. This can be expressed with finding all stabilizing controllers for which a value $\gamma > \gamma_{\min}$ in

$$\|\mathcal{F}_\mathcal{L}(P,K)\|_\infty < \gamma \tag{9}$$

can be achieved. By iterating using the algorithm presented in [7], γ can be iteratively reduced and an optimal solution is approached. This can either be solved according to [7, 20] by using an algebraic Riccati equation, as summed below, or via linear matrix inequalities, which is described in [22]. $K(s)$ is a stabilizing controller such that $\|\mathcal{F}_\mathcal{L}(P,K)\|_\infty < \gamma$ if, and only if

(i) $X_\infty \geq 0$ is a solution to the Riccati equation

$$A^TX_\infty + X_\infty A + C_1^TC_1 + X_\infty(\gamma^{-2}B_1B_1^T - B_2B_2^T)X_\infty = 0 \tag{10}$$

such that $\Re(\lambda_i)\left[A + (\gamma^{-2}B_1B_1^T - B_2B_2^T)X_\infty\right] < 0 \quad \forall i$,

(ii) $Y_\infty \geq 0$ is a solution to the Riccati equation

$$A^TY_\infty + Y_\infty A + C_1^TC_1 + Y_\infty(\gamma^{-2}C_1^TC_1 - C_2^TC_2)Y_\infty = 0 \tag{11}$$

such that $\Re(\lambda_i)\left[A + Y\infty(\gamma^{-2}C_1^TC_1 - C_2^TC_2)\right] < 0 \quad \forall i$,

(iii) $\rho(X_\infty, Y_\infty) < \gamma^2$

All resulting controllers are given by $K = \mathcal{F}_{\mathcal{L}}(K_c, Q)$, where

$$K_c(s) \overset{S}{=} \left[\begin{array}{c|cc} A_\infty & -Z_\infty L_\infty & Z_\infty B_2 \\ \hline F_\infty & 0 & I \\ -C_2 & I & 0 \end{array}\right] \tag{12}$$

$$F_\infty = -B_2^T X_\infty, \quad L_\infty = -Y_\infty C_2^T, \quad Z_\infty = (I - \gamma^{-2} Y_\infty X_\infty)^{-1} \tag{13}$$

$$A_\infty = A + \gamma^{-2} B_1 B_1^T X_\infty + B_2 F_\infty Z_\infty L_\infty C_2 \tag{14}$$

with $Q(s)$ being any stable proper transfer function for which $\|Q\|_\infty < \gamma$ holds. For choosing $Q(s) = 0$, we obtain the "central" controller which has exactly the same number of states as the generalized plant P:

$$K(s) = K_{c_{11}}(s) = -F_\infty(sI - A_\infty)^{-1} Z_\infty L_\infty. \tag{15}$$

This controller can be separated into a state estimator (observer) $\hat{x}$ and a state feedback u which are expressed as

$$\dot{\hat{x}} = A\hat{x} + B_1 \underbrace{\gamma^{-2} B_1^T X_\infty \hat{x}}_{\hat{w}_{\text{worst}}} + B_2 u + Z_\infty L_\infty (C_2 \hat{x} - y) \tag{16}$$

$$u = F_\infty \hat{x}. \tag{17}$$

The structure of this observer is similar to a Kalman filter, but contains an additional term $B_1 \hat{w}_{\text{worst}}$, which can be interpreted as an estimate of the worst-case disturbance (exogenous input). Iterations start at a default value $\gamma_{\max}$ and will reduce the costs γ until a minimal tolerance is reached, i.e. the algorithm converged. The method described above can be found for the general case without simplifications in [23] and is basis for the `MATLAB hinfsyn` function. In contrast to the original control design, only an additional, constant weight W_y was introduced in Fig. 5 / Eq. (5), which weighs the root bending moment of the vertical tail in z_y. With this adjustment, the sensitivity and complimentary sensitivity functions in Fig. 6 result for the novel lateral controller for the DLR HALE aircraft. It can be seen, that especially in the lateral acceleration channel, the complimentary sensitivity is reduced, which can be expected since lateral acceleration and VT root bending are closely coupled via the rudder input channel of the aircraft.

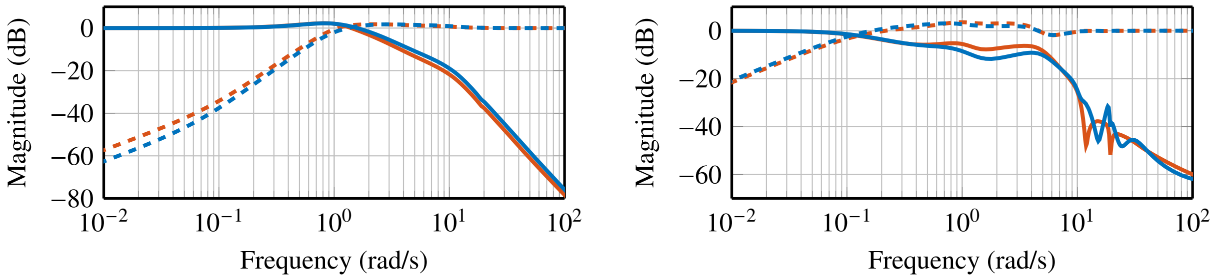

(a) Roll attitude channel.

(b) Lateral acceleration channel.

Fig. 6 Sensitivity (- - - , - - -) and complimentary sensitivity (——, ——) functions of the $\mathcal{H}_\infty$ controller (——, - - -) versus the initial controller (——, - - -) at the design velocity of $\mathbf{V_{eas}}$ = 9 m/s.

IV. Design Verification Using 1-Cosine Gust Inputs

In this section the analysis results of the novel FCS design using the non-linear aircraft model described in Sec. II and worst-case 1-cosine gust inputs. Besides the aircraft's equations of motion, the non-linear model also contains sensor and actuator models.

A. Worst Case Analysis

In Fig. 7, the rigid body response of the initial roll controller, designed without consideration of the VT root bending moment, is compared to the novel controller. The simulation scenario is the worst-case gust defined by the maximum VT root bending moment selected in Fig. 4b. By comparing the red and blue curves, it can be seen that the rigid body reaction is nearly the same for roll rate and attitude. The peaks in lateral load factor N_y and yaw rate are reduced. Regarding the control surface action, the aileron command is the same for both controllers, with all ailerons in saturation. The rudder, however, is commanded in the opposite direction as in the initial design which is assumed to be caused by the slightly lower controller bandwidth in the lateral acceleration channel. Analyzing the VT root bending moment M_x in Fig. 8 reveals a reduction of the second peak which is the largest absolute value, by about 28% compared to the initial controller. Furthermore, a reduction of almost 10% in M_x compared to the open loop could be achieved.

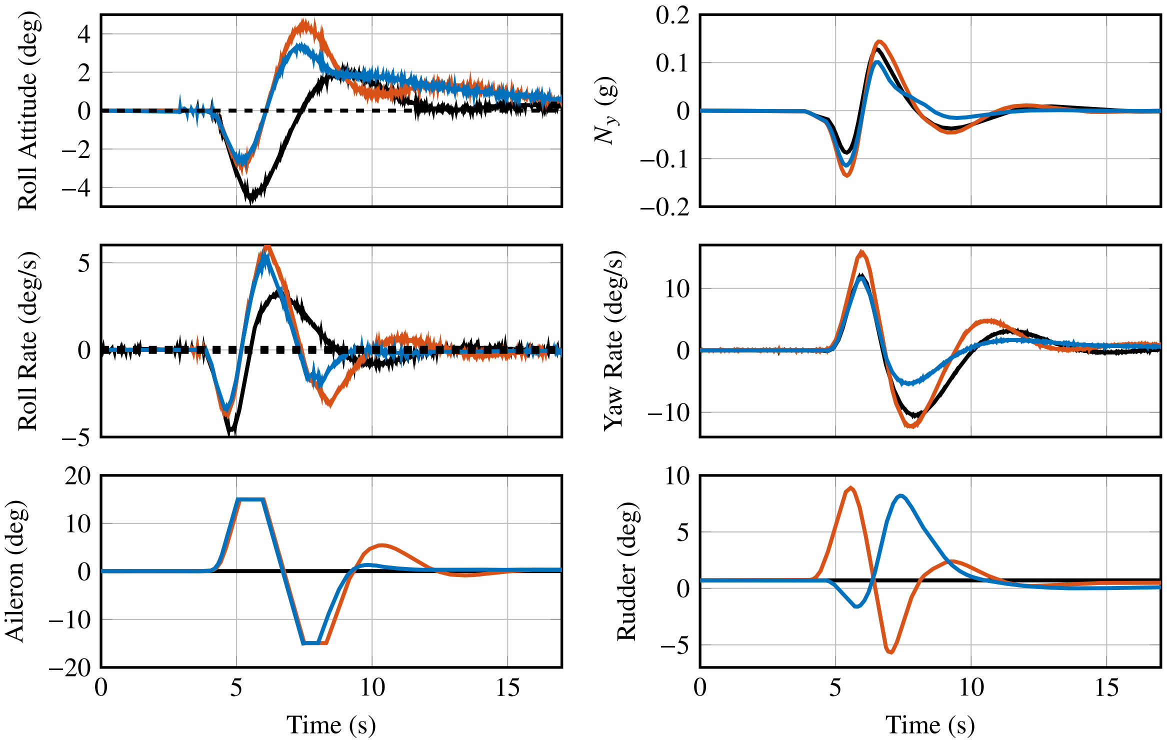

Fig. 7 Rigid body modes' response to a 1-cosine gust for the initial (——), M_x reduction controller (——) and open loop (——). Gust gradient length of 9 m and gust direction in body y-axis, at sea level and V_{eas} = 11 m/s.

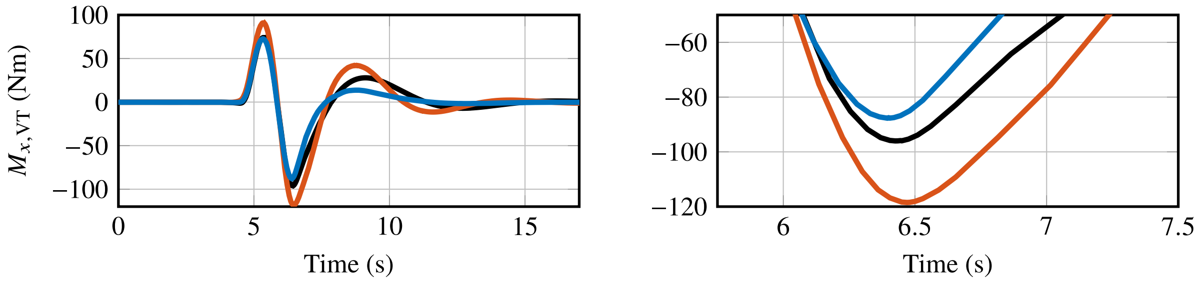

Fig. 8 Root bending moment M_x of the VT during a discrete 1-cos gust excitation at sea level & V_{eas} = 11 m/s using the initial FCS (——), open loop (——), novel FCS (——). Right hand side: zoom onto peak values.

B. Monte-Carlo Based Verification

For further validation of the novel flight controller, the initial and novel FCS designs are compared in a Monte-Carlo simulation. The main varying parameters are the gust gradient (5 - 100 m) and the gust direction (left and right side). Furthermore, the operating point is varied inside the operational flight envelope (altitude 0-20 km, V_{eas} 9 - 11 m/s). The same non-linear simulator as in the previous discussion is used. Note that the results (in terms of section loads) of this analysis are similar but not identical to those shown in Sec. II.D, Fig. 4b, because different load cases are considered. The aim of the analysis in this section is to verify the functionality of the FCS over a large range of operational points and demonstrate the robustness of the proposed solution. For the latter a risk analysis on the VT root bending moment exceeding an absolute value of 100 Nm is performed. Figure 9 shows the cumulative density function (CDF) of the highest achieved VT root bending moment within each simulation for a set of $n = 5000$ sample simulations. For the initial controller (Fig. 9a), it can be seen that the maximum observed root bending moment $M_{x,\mathrm{VT}}$ is approx. 145 Nm, while the maximum value for the novel controller is only 110 Nm. The defined limit of 100 Nm is violated in 20% of the simulation cases with the initial controller, but only in 1.5% of the novel controller simulation cases which is a reduction of more than 90%. Summarizing the findings from Fig. 9: the maximum root bending moment $M_{x,\mathrm{VT}}$ seen in all simulation cases has been lowered by 24% from 145 Nm to 110 Nm and the probability of exceedance for values greater than 100 Nm has been lowered from 20% to 1.5% for the given sample size of $n = 5000$. Similar to Fig. 4b, the plot of the minimum and maximum values of the root bending moment of the VT can be combined with the torsional moment of the VT ($M_{z,\mathrm{VT}}$) in a load envelope. The resulting envelopes are shown in Fig. 10. Figure 10a shows the initial controller's envelope for the gust encounter cases only (vs. all investigated load cases in Fig. 4b). Figure 10b shows the novel load envelope and the comparison to the initial controller (- - -) and open loop convex hulls (- - -) respectively. As previously discussed, the maximum bending moment is significantly reduced. Moreover, even an improvement in M_x compared to the open loop gust encounter is achieved (- - - vs. - - - envelope in Fig. 10b). On the downside, the cost for the reduction of the bending moment is an increase in VT torsional moment by approx. 15% (39 Nm for the initial to 45 Nm in magnitude for the novel controller). Since the primary structure of the VT is defined by a minimum manufacturable material thickness, that increase is acceptable. Additionally, the effect of the FCS during lateral gust encounter on other load monitoring stations throughout the aircraft has been assessed. Exemplary in Fig. 10c the wing root bending vs. torsional moment envelope is depicted for both controllers. Differences of approx. 1% are observed (less torsional moment with the novel controller) which lead to the assumption that the influence of the novel flight controller discussed in this paper is negligible on the wing loads compared to the initial design. This assumption will be verified in an upcoming analysis of loads at all monitoring points of the aircraft.

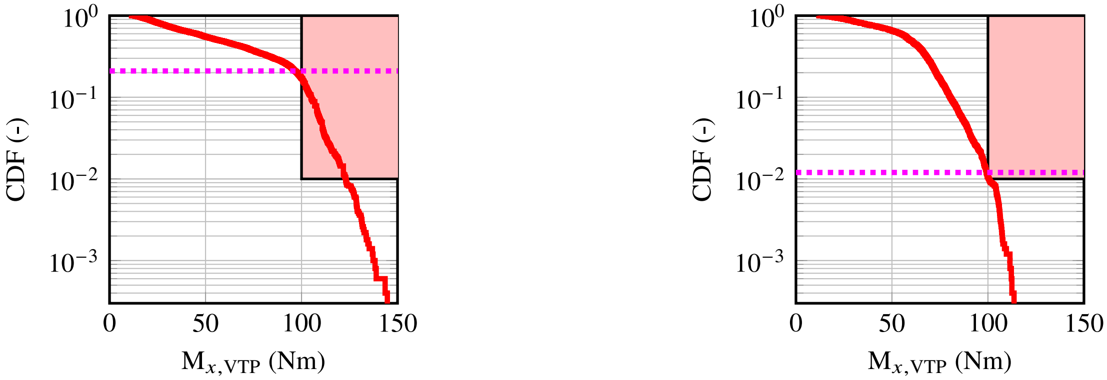

(a) Initial Controller. **(b) Novel controller.**

Fig. 9 CDF of the maximum VT root bending moment for both controllers.

C. Sensor Noise and Time Delays

The results in the previous section were taking into account only actuator and sensor models but not yet time delays and sensor noise. An additional Monte-Carlo run has been conducted, which highlights the effects of time delays on the closed loop dynamics and loads. In Fig. 10d the load envelopes of the VT root bending moment vs. torsional moment are depicted under the influence of realistic assumptions (approx. 100 ms total delay time). The results show that for

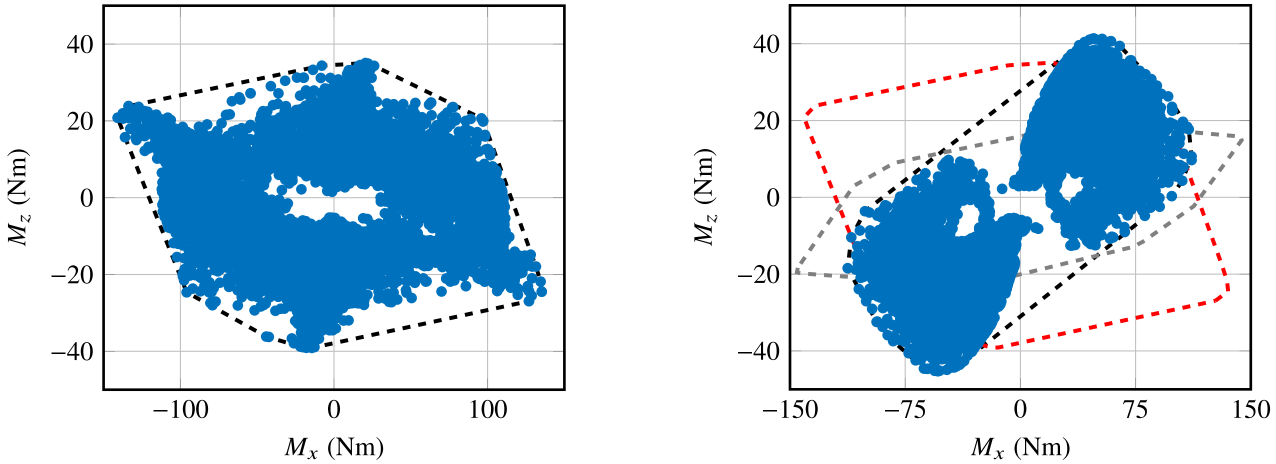

(a) VT root bending vs. torsional moment for the initial controller.

(b) VT root bending vs. torsional moment for the novel controller and load envelope (- - -) compared to the envelopes of the initial controller (- - -) and open loop (- - -).

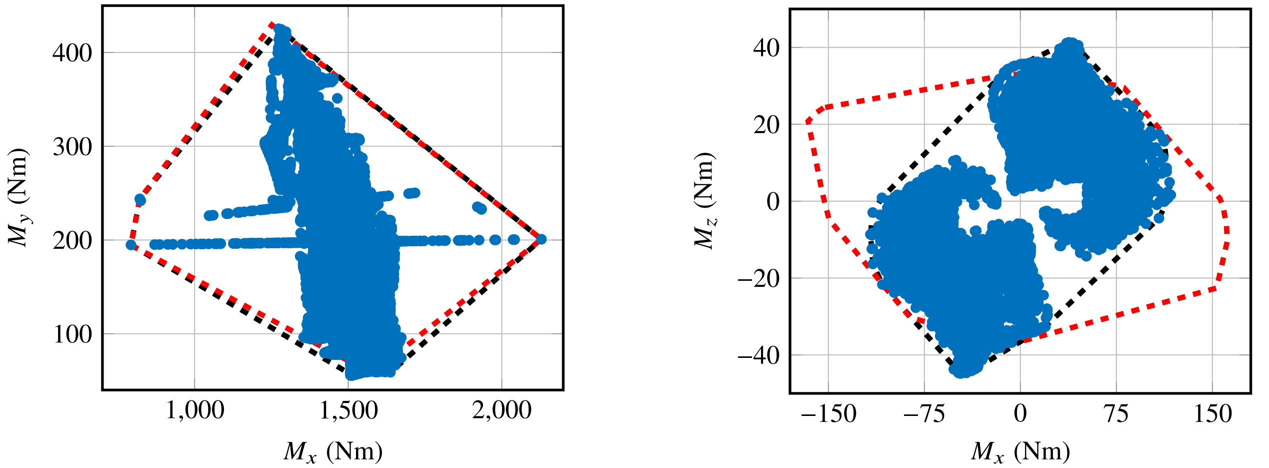

(c) Wing root bending vs. torsional moment of the novel controller and load envelope (- - -) compared to the envelope of the initial controller (- - -).

(d) VT root bending moment for the novel controller (- - -) vs. envelope of the initial controller (- - -) taking into account sensor and delay effects.

Fig. 10 Load envelopes for the initial and novel lateral axis flight controller for lateral worst case gusts.

both controllers the maximum torsional moment is similar to the scenarios without delay in Fig. 10b. In contrast, the maximum absolute root bending moment rises by approx. 17% (from 140 Nm to 165 Nm) for the initial controller. For the novel controller, the increase in VT root bending has an amount of only 4% (112 Nm without and 117 Nm with delay). This backs the assumption that the novel controller is more robust to uncertainties and the presented technology should be assessed for further critical load monitoring stations.

V. Conclusion

This paper presented a robust, multi-variable controller design for the lateral axis of a HALE aircraft which can significantly reduce (-24%) the peak loads of the root bending moment at the vertical tail compared to an initial controller. Moreover, the presented approach enables the control engineer to tune the control law in such a way, that the peak loads at the selected monitoring stations stay close to or even below the open loop peak loads. This delivers an important contribution in order to enable a light weight aircraft structural design and has the potential to enable further reduction of the structural weight of the presented example aircraft.

Acknowledgments

The presented work is part of the DLR's High Altitude Platform (HAP) project. Currently there are 17 DLR Institutes involved in the project. The authors would like to thank especially their colleagues from the institutes of Aerodynamics and Flow Technology, Composite Structures and Adaptive Systems and Flight Systems for providing the aircraft models and data used for this research.

References

[1] Noll, T. E., Brown, J. M., Perez-Davis, M. E., Ishmael, S. D., Tiffany, G. C., and Gaier, M., "Investigation of the Helios Prototype Aircraft Mishap," Tech. rep., NASA, 2004.

[2] Airbus, "Zephyr S set to break aircraft world endurance record," , 07/2018. URL `https://www.airbus.com/defence/uav/zephyr.html#introduction`.

[3] Nikodem, F., and Bierig, A., "DLR HAP - Herausforderungen in der Entwicklung der Höhenplattform und ihrer Anwendungen," *Deutscher Luft- und Raumfahrtkongress (DLRK)*, 2020.

[4] Weiser, C., and Ossmann, D., "Baseline Flight Control System for High Altitude Long Endurance Aircraft," *AIAA SciTech 2022 Forum*, American Institute of Aeronautics and Astronautics, 2022. doi: https://doi.org/https://arc.aiaa.org/doi/10.2514/6.2022-1390.

[5] Weiser, C., and Ossmann, D., "Fault-Tolerant Control for a High AltitudeLong Endurance Aircraft," *11th IFAC Symposium on Fault Detection, Supervision and Safety for Technical Processes - SAFEPROCESS*, 2022.

[6] Weiser, C., Ossmann, D., and Pfifer, H., "Robust Path-following Control with Anti-Windup for HALE Aircraft," *30th Mediterranean Conference on Control and Automation*, 2022. doi: https://doi.org/10.1109/MED54222.2022.9837232.

[7] Doyle, J. C., and Glover, K., "State-space solutions to standard H2 and H∞ control problems," *IEEE Transactions on Automatic Control*, Vol. 34, No. 8, 1989.

[8] Voß, A., Handojo, V., Weiser, C., and Niemann, S., "Results from Loads and Aeroelastic Analyses of a High Altitude, Long Endurance, Solar Electric Aircraft," *Journal of Aeroelasticity and Structural Dynamics*, Vol. 9, No. 1, 2022, pp. 1–22.

[9] Voß, A., Koch, C., Niemann, S., Handojo, V., and Weiser, C., "Transition From Preliminary to Detailed Design of a Highly Elastic Solar Electric Aircraft," *International Forum on Aeroelasticity and Structural Dynamics (IFASD)*, 2022.

[10] Kier, T., and Hofstee, J. W., "Varloads - Eine Simulationsumgebung zur Lastenberechnung eines voll flexiblen, freifliegenden Flugzeugs," *Deutscher Luft- und Raumfahrtkongress (DLRK)*, 2004.

[11] Waszak, M., Buttrill, C., and Schmidt, D., "Modeling and Model Simplification of Aeroelastic Vehicles: An Overview," Tech. rep., NASA, 02 1997.

[12] Voß, A., Handojo, V., Weiser, C., and Niemann, S., "Preparation of Loads and Aeroelastic Analyses of a High Altitude, Long Endurance, Solar Electric Aircraft," *Aerospace Europe Conference*, 2020.

[13] Voß, A., "An Implementation of the Vortex Lattice and the Doublet Lattice Method," Tech. Rep. DLR-IB-AE-GO-2020-137, Institut für Aeroelastik, Deutsches Zentrum für Luft- und Raumfahrt, 2020.

[14] Kier, T., and Looye, G., "Unifying Manoeuvre and Gust Loads Analysis," *International Forum on Aroelasticity and Structural Dynamics (IFASD)*, 2009.

[15] anon., "Certification Specifications for Large Aeroplanes CS-25," Tech. rep., European Aviation Safety Agency (EASA), 2007.

[16] Schulz, S., and Ossmann, D., "Estimation of Global Structural Aircraft Loads due to Atmospheric Disturbances for Structural Fatigure Estimation," *International Forum on Aroelasticity and Structural Dynamics (IFASD)*, 2022.

[17] Hoblit, F. M., *Gust Loads on Aircraft: Concepts and Applications*, American Institute of Aeronautics and Astronautics, 1988. doi: https://doi.org/10.2514/4.861888.

[18] Brockhaus, R., Alles, W., and Luckner, R., *Flugregelung*, Springer, 2001.

[19] Andry, A. N., Shapiro, E. Y., and Chung, J., "Eigenstructure Assignment for Linear Systems," *IEEE Transactions on Aerospace and Electronic Systems*, Vol. AES-19, No. 5, 1983, pp. 711–729. doi: https://doi.org/10.1109/TAES.1983.309373.

[20] Skogestad, S., and Postlethwaite, I., *Multivariable Feedback Control*, John Wiley & Sons, 2005.

[21] Theis, J., Pfifer, H., and Seiler, P., "Robust Modal Damping Control for Active Flutter Suppression," *Journal of Guidance, Control, and Dynamics*, Vol. 43, No. 6, 2020, pp. 1056–1068. doi: https://doi.org/10.2514/1.g004846.

[22] Gahinet, P., and Apkarian, P., "Structured H_∞ Synthesis in MATLAB," *IFAC Proceedings Volumes*, Vol. 44, No. 1, 2011, pp. 1435–1440. doi: https://doi.org/10.3182/20110828-6-IT-1002.00708.

[23] Glover, K., and Doyle, J. C., "State-space formulae for all stabilizing controllers that satisfy an H_∞-norm bound and relations to risk sensitivity," *Systems & Control Letters*, Vol. 11, 1988, pp. 167–172.